Current Biology 20, 979–988, June 8, 2010 ©2010 Elsevier Ltd All rights reserved DOI 10.1016/j.cub.2010.04.040

Article

Cell-Length-Dependent Microtubule Accumulation during Polarization

Dominique Seetapun[1] and David J. Odde[1,*]
[1]Department of Biomedical Engineering, University of Minnesota, Minneapolis, MN 55455, USA

Summary

Background: Breaking cell symmetry, known as polarization, requires dynamic reorganization of microtubules (MTs) and is essential to many cellular processes, including axon formation in neurons. A critical step in polarization is believed to be the "selective stabilization" of MTs, which hypothesizes a spatial and/or temporal shift toward net MT assembly in a preferred direction of growth.
Results: We now find that a simpler "length-dependent" model, in which MT assembly parameters are spatially and temporally constant, predicts MT accumulation in the direction of growth because of longer mean first passage times in the longer direction. We experimentally tested both models by tracking MT assembly dynamics in polarizing embryonic chick forebrain neurons, and we confirmed that assembly is spatially and temporally constant during axon formation.
Conclusion: Cell polarization occurs most simply through cell-length-dependent accumulation of MTs without MT stabilization or capture. In this way, F-actin-mediated cell shape and size changes can be read out by dynamic MTs undergoing simple dynamic instability to ultimately break cell symmetry.

Introduction

Understanding cell polarization is essential to understanding stem cell division, tumor metastasis, and neuronal development [1]. A dramatic example of symmetry breaking is neuron polarization, in which a single axon is selected from a set of minor processes (MPs) to subsequently form synaptic connections with other neurons. Establishing cell polarity requires that dynamic microtubule (MT) plus ends undergo reorganization via dynamic instability (DI) [2] to preferentially accumulate in the preferred direction (e.g., toward the nascent axon) [3–6]. During DI, MT plus ends stochastically switch between net growth and net shortening phases. In neurons, the selective stabilization model (SSM) hypothesizes that MTs are specifically recruited to the polarized axon by selective stabilization via a gradient in MT dynamics or capture of dynamic MT plus ends that stochastically enter the axon from the cell body (Figures 1A–1C) [3–5, 7, 8].

By constructing a simpler polarization model, we found that MTs will accumulate in longer neurites, MPs or axons, without any selective stabilization. This cell-length-dependent model (CLDM) correctly predicts the number, distribution, and turnover of MTs in both MPs and axons in cultured primary neurons. To test the SSM and CLDM, we conducted a detailed quantitative analysis of MT dynamics in polarizing embryonic chick forebrain neurons (ECFNs) via fluorescence microscopy imaging of EGFP-EB1 and EGFP-α-tubulin distributions and dynamics. We found that MT accumulation during neuron polarization does not exhibit selective stabilization of MTs, whereas the CLDM may be a general mechanism underlying cell polarization.

*Correspondence: oddex002@umn.edu

Results

Simple MT Dynamic Instability Model

Before testing the SSM, we first constructed a simpler stochastic model of MT DI in neurites and used the model to make testable predictions for the ECFN system. We constructed a base model without any spatiotemporal changes in parameter values. This base model assumes that a neurite of length $L_{neurite}$ has a cylindrical shaft of uniform caliber and a growth cone at the distal end (Figures 2A and 2B). Multiple independent MTs undergo DI within the neurite, with centrosomally attached MTs entering the neurite from the cell body by plus-end polymerization and exiting to the cell body by depolymerization. The new MTs arrive anterogradely oriented (i.e., plus ends pointing away from the cell body) at rate $k_{arrival}$. MTs grow out of the neurite shaft into the growth cone, and MTs that polymerize to the growth cone edge immediately undergo catastrophe, as observed experimentally (data not shown). Further complexities can be added to the base model, such as spatial or temporal MT regulation or MT nucleation (see below). To characterize the state of the MTs in the system, we can calculate the drift velocity (V_D; Figure 2C) with the four MT DI parameters: growth (V_g) and shortening (V_s) rates, catastrophe (k_c), and rescue frequencies (k_r). The drift velocity is the net MT length change per unit time [9–12]. Depending on the sign of the drift velocity, we can determine whether the MT plus ends are biased toward net shortening ($V_D < 0$), net growth ($V_D > 0$), or neither ($V_D = 0$).

MTs Accumulate in a Cell-Length-Dependent Manner

Using the base model of simple MT DI with $V_D = 0$, such that plus ends execute a random walk (Figures 2D and 2E), we found that the model predicts an ~3-fold increase in the number of MTs in the neurite with a 3.5-fold increase in neurite length as a neurite grows in length from 10 μm (average MP length) to 35 μm (average axon length; Figure 2F). This can be explained simply by the increased neurite length the MTs have to explore in the axon as compared to MPs: the longer the space, the longer the time it takes, on average, for the randomly walking MT plus ends to exit the space (i.e., the mean first passage time increases monotonically with the length of the space [13]). Because there is a constant arrival rate and a length-dependent departure rate, the number of MTs at steady state increases monotonically with increasing neurite length. Such length-dependent MT accumulation could potentially provide a simple mechanism for axon specification: the longer the neurite, the more MTs it will have, which increases the probability for more elongation-promoting components to be transported toward the growth cone in an MT-dependent manner (e.g., via microtubule-based motors). This CLDM could explain MT reorientation during cell polarization more generally.

To determine whether cell-length-dependent MT accumulation could be observed experimentally, we estimated the

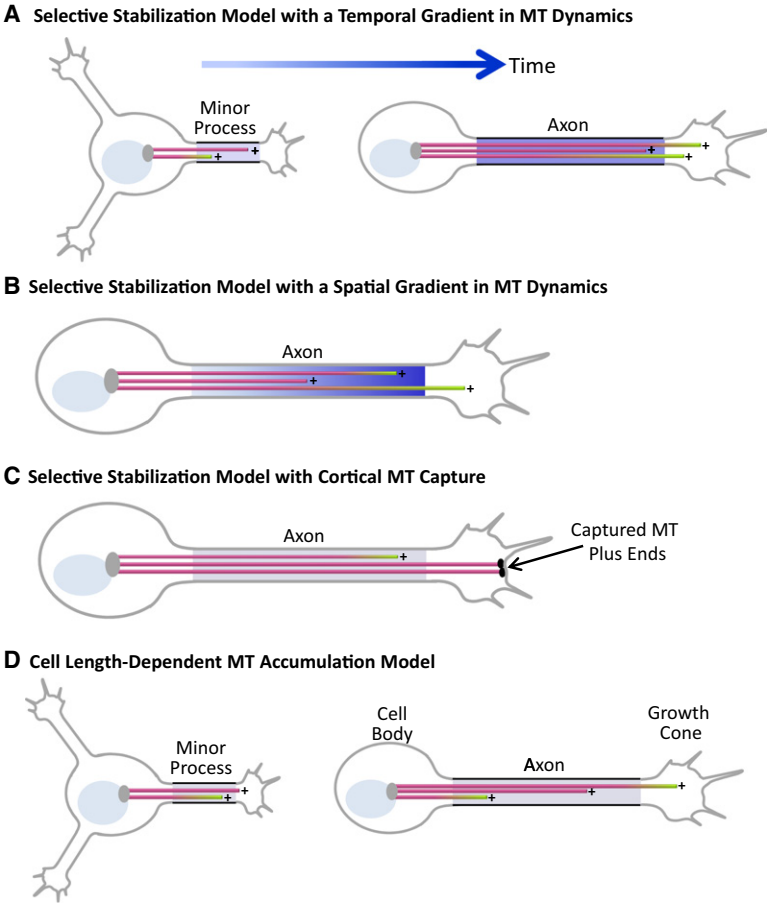

Figure 1. Comparison of the Selective Stabilization and Cell-Length-Dependent Models

(A–C) The selective stabilization model (SSM) can be interpreted in three different ways: (1) with a temporal gradient in microtubule (MT) dynamics (A), (2) with a spatial gradient in MT dynamics (B) [7], or (3) with MT capture (C) [5]. During neuron polarization, the SSM predicts a shift toward net MT assembly in space and/or time as one minor process elongates faster than the others to then become the axon. The SSM with a temporal gradient (A) predicts a shift toward net MT assembly during neuron polarization as one of the minor processes (MPs) elongates to become the axon. The SSM with a spatial gradient (B) predicts a shift toward net MT assembly within the MP or within the axon near its growth cone (GC). The SSM with MT capture (C) predicts MT capture at or near the growth cone, thus preventing MT dynamic instability from occurring. This could occur through a proposed MT capping protein.

(D) In contrast to any of the SSM scenarios, the cell-length-dependent model (CLDM) predicts an increase in MT number without a change in MT dynamic instability parameters during neuron polarization. In the CLDM, because there is a constant MT arrival rate but a length-dependent departure rate, MTs accumulate naturally in longer neurites.

number of MTs at the proximal base of the neurite near the cell body with cultured ECFNs [14] transfected with pEGFP-α-tubulin (note that ECFNs were transfected with plasmids via in ovo electroporation, which allows for expression of proteins prior to plating, making it unlikely that a subpopulation of MTs exist that are completely unlabeled). Consistent with the CLDM model, we measured an ~3.5-fold increase in the number of MTs in MPs as compared to axons, 27.8 ± 3.4 MTs and 90.0 ± 8.0 MTs (mean ± standard error of the mean [SEM], n = 42 MPs, 17 axons), respectively, as the average neurite length increased 3.5-fold (Figure 2G). We found a positive correlation between neurite length and MT number for MPs ($p = 0.004$) and axons ($p = 0.007$), respectively. We also found a significant positive correlation over all neurites, MPs, and axons ($p = 10^{-14}$). Similar MT numbers were obtained in untransfected cells when measured from tubulin immunolabeled samples (data not shown). These results show that the accumulation of MTs in axons observed in ECFNs, and previously in hippocampal neurons [15], could be attributed simply to an increase in neurite length and not necessarily to any spatiotemporal change in MT plus-end assembly or cortical plus-end capture.

MT Dynamics Do Not Vary Spatially or Temporally during ECFN Polarization

To further test the CLDM, we systematically quantified the temporal and spatial changes in MT polymerization dynamics during neuron polarization through direct observation of MT assembly with pEGFP-EB1. This allowed us to reliably track individual EGFP-EB1 comets that label growing MT plus ends [16, 17]. EGFP-EB1 comets have an inherent asymmetry such that the brightest part of the comet indicates the MT plus-end location and the comet tail indicates the location of the MT lattice (Figure 3C), allowing for determination of MT orientation. The presence and localization of endogenous EB1 was verified through immunostaining of untransfected ECFNs (see Figure S1 available online).

Neurons were characterized temporally by their developmental stage, either unpolarized (stage 2) or polarized (early stage 3) [18], and spatially by their various cellular compartments during polarization: the cell body, MPs in stage 2 neurons, axons in stage 3 neurons, and growth cones (GCs) at the tips of MPs or axons (Figures 3A and 3B). Quantitative tracking of fluorescent EB1 comets allowed us to measure the growing MT plus-end velocity and lifetime as a function of spatial location in neurons before and after polarization (Movie S1). From these data, we were able to generate a spatiotemporal map of the MT dynamics during neuron polarization in vitro.

We found that comet velocity and lifetime were unaltered within the same compartment during neuron polarization. For example, we found that there was no significant difference ($p > 0.01$ from multiple comparison testing) between mean comet velocities in MPs and axons, 146 ± 3.2 nm/s (n = 131 comets) and 135 ± 2.7 nm/s (n = 159 comets), respectively (Figure 3D; mean ± SEM). The same was true for mean stage 2 and stage 3 cell body comet velocities and MP and axonal GC comet velocities (Figure 3D). Similarly, comet lifetimes did not change temporally or spatially during neuron polarization. On average, in every compartment of both unpolarized and polarized neurons, EB1 comets persisted for ~10 s (Figure 3E). In addition, we tested for spatial variation in comet velocities and lifetimes within neurites but did not find statistically significant differences (Figure S2). These results are in agreement with previously reported results for stage 3 hippocampal neurons [19]. In ECFNs, we also found that centrosome

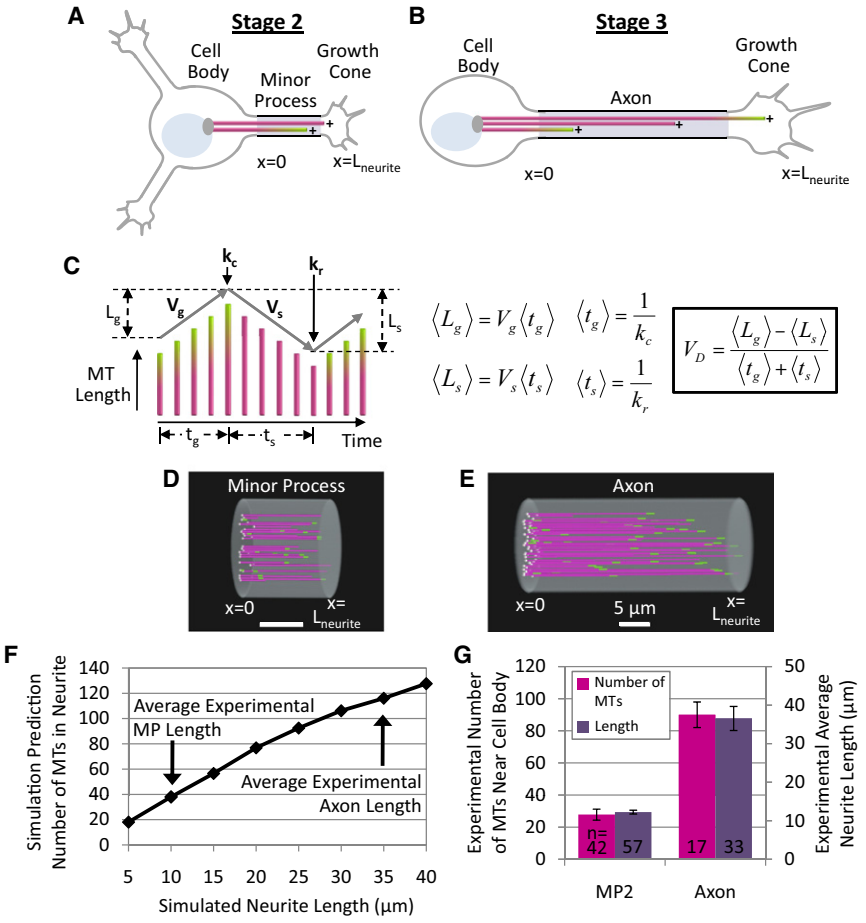

Figure 2. A Simple Model of MT Dynamic Instability Predicts Neurite-Length-Dependent MT Accumulation during Neuron Polarization

(A and B) During polarization, neurons transition from an unpolarized cell with multiple MPs (A) into a polarized cell with a single long axon (B). GCs are shown at the tips of the MPs and the axon. The centrosome is depicted as a gray oval, the nucleus as a blue oval, and the MTs as magenta bars. Growing MTs have green tips. The model applies to the neurite shaft, as indicated by the gray area.

(C) Diagram of an MT undergoing dynamic instability (DI) over time. Growing MTs have green tips and grow at rate V_g. MTs shorten at rate V_s. MTs can switch stochastically from growing to shortening, termed a catastrophe, with frequency k_c. Similarly, MTs can stochastically switch from shortening to growing, termed a rescue, with frequency k_r. The equations to calculate the average length added during growth, $< L_g >$, and lost during shortening, $< L_s >$, are shown on the right, along with the equations for the average time spent growing, $< t_g >$, and shortening, $< t_s >$. These quantities determine the MT drift velocity (V_D), which is the mean length added or lost per second of DI.

(D and E) Animation of the simple DI model in MPs (D) and axons (E) (see Movie S2). Green tips indicate growing MTs, and gray spheres indicate location of MT minus ends. Scale bar in (D) is 5 μm.

(F) The simple model of DI with $V_D = 0$ predicts a roughly 3-fold increase in the number of MTs with a 3.5-fold increase in neurite length from 10 μm to 35 μm (n = 40 simulations per neurite length). We refer to this simple DI model as the CLDM.

(G) Experimental data from EGFP-α-tubulin-expressing ECFNs demonstrates a 3.5-fold increase in MT number during polarization from an ~10 μm MP to an ~35 μm axon, including growth cones. This closely matches the model-predicted 3-fold increase in MT number. The number of neurites measured is shown in the bars. Data shown are mean ± standard error of the mean (SEM).

positioning did not correlate with axon positioning or with the length of the neurite (Figure S3).

Although we failed to detect any temporal change in EB1 comet dynamics, we found that GC comet velocities were 36% slower on average than neurite comet velocities (Figure 3D). Recent work [20] demonstrates the presence of actin retrograde flow in ECFN GCs, and through quantitative analysis we were able to attribute the decreased EB1 comet velocities in GCs entirely to transient MT plus-end coupling to actin retrograde flow, and not to a decrease in MT polymerization (Figure S4). The measured average MT transport rate in growth cones was −42 nm/s, which accounts quantitatively for the decreased EB1 comet velocity in the growth cone. These data are again consistent with a lack of spatial control over MT assembly during neuron polarization.

Furthermore, we examined EB1 comet densities per area and per length of neurite. Interestingly, even though axons were 3.5-fold longer than MPs on average, the number of comets per length of neurite was the same ($p = 0.13$) regardless of polarization state, 1.10 ± 0.62 (n = 10 cells, 32 MPs) and 1.40 ± 0.49 (n = 10 cells, mean ± standard deviation [SD]) comets/μm for MPs and axons, respectively. The same was true for comet densities per area of neurite (data not shown). We also did not detect, via EGFP-α-tubulin fluorescence recovery after photobleaching (FRAP), any evidence of MT transport in neurites (Figure S5). The lack of temporal control over EB1 comet velocity and lifetime, combined with similar EB1 comet densities in all compartments regardless of neuron polarization, indicates that MT polymerization rates are not upregulated temporally and that MTs are recruited to the axon after polarization as a natural consequence of the increase in neurite length (CLDM) and not due to biases in MT assembly (SSM).

Polarizing ECFN MTs Are Weakly Biased toward Net Shortening

To determine whether the CLDM could fully explain the increase in MT number during polarization in the absence of spatial or temporal changes in MT assembly dynamics, we simulated both MPs and axons by using measured MT growth rates and lifetimes. Because only two of the four DI parameters could be directly measured (V_g and k_c), we treated V_s and k_r as adjustable parameters, with V_s set to a value measured in growth cones that was corrected for average transport (Figure S6). By adjusting k_r, we could then reproduce all three regimes of DI: net shortening ($V_D < 0$; Figures 3F and 3G), balanced growth and shortening ($V_D = 0$; Figure 3H), and net growth ($V_D > 0$; Figure 3I). We found the EB1 distribution (Figure 3J) to be a very sensitive indicator of which regime the MT array was operating in, with decaying, uniform, and increasing EB1 distributions corresponding to net shortening, balanced growth and shortening, and net growth, respectively.

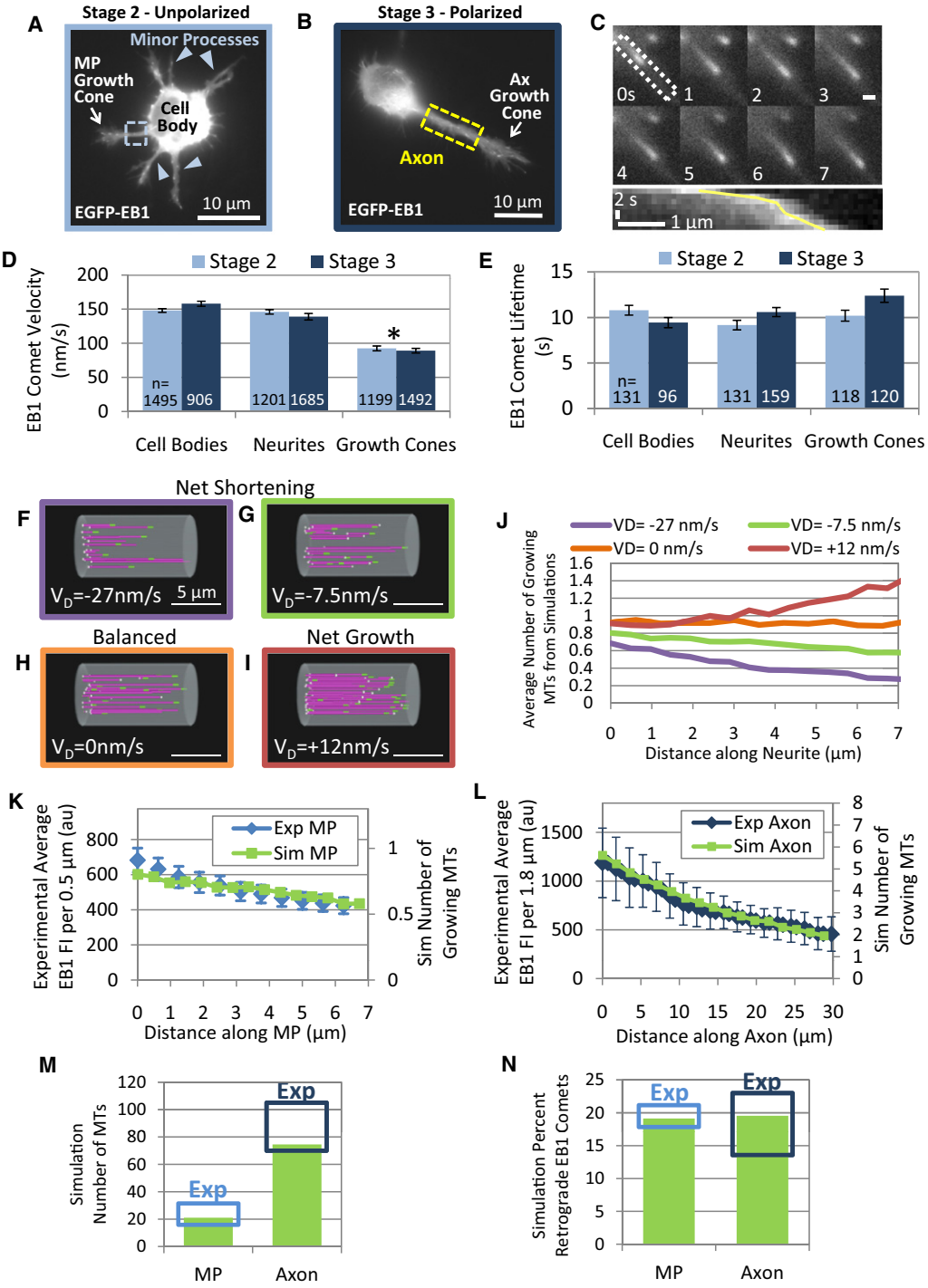

Figure 3. Neurons Do Not Exhibit Spatial-Temporal Control over MT Assembly during Polarization

(A and B) EGFP-EB1-expressing ECFNs in stage 2 (unpolarized) and stage 3 (polarized). Unpolarized neurons have multiple shorter MPs (dotted blue box and arrow heads), whereas polarized neurons have a single longer axon (dotted yellow box).

(C) Montage of an EB1 comet moving anterogradely in the axonal growth cone of an ECFN. Scale bar is 1 µm. Dotted box indicates region used to create the kymograph shown directly below the montage. This EB1 comet has an estimated mean velocity of 169 nm/s and a lifetime of 7 s. Yellow line indicates the position of the brightest part of the comet.

(D and E) Experimentally measured EB1 comet velocities and EB1 comet lifetimes in unpolarized (light blue) and polarized (dark blue) neuron compartments. There was no significant difference in MT assembly, MT growth rate, or MT lifetime during polarization. The lower EB1 comet velocity in GCs versus axons or cell bodies (*$p < 0.01$) is due to local mechanical coupling between MTs and F-actin retrograde flow, and not to a decrease in MT assembly rates (Figure S4). Data shown are mean ± SEM. The number of instantaneous velocity measurements is shown in the bars in (D), with the corresponding number of MTs for (D) and (E) shown in the bars in (E).

(F–I) Animation depictions of simulations, which include MT nucleation within the neurite, with overall net MT shortening (F and G), balanced growth and shortening (H), and net growth (I). Via changes in k_r, varying drift velocities (V_D) are shown in each case. The final simulation V_D value for ECFNs is shown in (G). All scale bars in (F)–(I) are 5 µm.

Table 1. Cell-Length-Dependent Model Parameters with Nucleation

	V_g (nm/s)	V_s (nm/s)	k_c (s^{-1})	k_r (s^{-1})	k_{nuc} ($s^{-1}\mu m^{-1}$)	$k_{arrival}$ (s^{-1})
MP	150	250	0.1	0.154	0.0086	0.22
Axon	150	250	0.1	0.154	0.0086	0.40

V_g, V_s, k_c, and $k_{arrival}$ were constrained to be within 2 × SEM of experimental values. k_{nuc} was constrained by experimental measurements of the percentage of retrograde EB1 comets. k_r was the only adjustable parameter. The following abbreviations are used: V_g, growth; V_s, shortening velocities; k_c, catastrophe; k_r, rescue frequencies; k_{nuc}, nucleation rate; $k_{arrival}$, arrival rate.

To incorporate the MTs arriving from the cell body, we fixed the arrival rate, $k_{arrival}$, so that they were within the 95% confidence interval (CI) of the experimental arrival rates (Table 1). From our experiment, we found that $k_{arrival}$ was 1.7-fold higher in axons, 0.24 ± 0.13 s^{-1} (n = 12 cells, 29 MPs) and 0.36 ± 0.12 s^{-1} (n = 10 cells, mean ± SD) for MPs and axons, respectively, which can be attributed to a wider neurite neck, where the neurite extends from the cell body. Axons had a statistically wider neurite neck ($p = 10^{-6}$) than MPs, 1.5 ± 0.65 μm and 3.0 ± 0.81 μm in MPs (n = 65) and axons (n = 17, mean ± SD), respectively. Although a wider neurite neck is not necessarily the only explanation for the increased $k_{arrival}$ in axons, it does make good physical sense. Using the experimentally observed values for V_g, V_s, k_c, and $k_{arrival}$, we adjusted k_r such that the simulation best fit the decaying experimental EB1 distributions in MPs and axons (Figures 3K and 3L). We also included an adjustable nucleation rate, k_{nuc}, to account for our experimental observation of retrogradely oriented EB1 comets (19.3% in MPs and 18.8% in axons; Figure 3N; Table 1). The resulting DI parameter set had all the same input parameters except for $k_{arrival}$ (Table 1). The DI parameter set operated in the net shortening regime but was very close to balanced growth and shortening with $V_D = -7.5$ nm/s (Figures 3G and 3J; Movie S2). This means that, as a population, MTs are losing −7.5 nm/s, which is offset by both nucleated MTs and those arriving from the cell body.

CLDM with Nucleation Predicts Polarizing ECFN MT Distributions and Number

Using the MP DI parameters and the experimentally measured axonal EB1 arrival rate, we increased the simulated neurite length to the average axon length and found that the simulation was able to predict a priori, without parameter adjustment, the decaying EB1 distribution (Figure 3L), the correct number of MTs (Figure 3M), and the percentage of retrograde EB1 comets in axons (Figure 3N). This simple DI model was also able to reproduce the dramatic 3.5-fold increase in MT number simply through a 3.5-fold increase in neurite length. Retrograde EB1 distributions (Figures S7A and S7B), as well as decaying MT distributions observed in MPs and axons, were also reproduced by the model (Figures S7C and S7D). In addition, the model predicted the absolute number and linear density of growing MTs, as measured by EGFP-EB1. Simulations also show that the distribution of cell-body-derived MTs mirrors the overall distribution of MTs, with the distribution of nucleated MTs having a minor contribution (data not shown). We noted that the 50% increase in observed MT arrival rate in axons versus MPs (0.36 versus 0.24 s^{-1}, respectively) led to a 1.7-fold increase in simulated MT number, which was insufficient by itself to explain the observed 3.5-fold increase. However, together with the 3.5-fold increase in neurite length, the 1.7-fold increase in arrival rate allowed the CLDM to quantitatively predict the experimentally observed 3.5-fold increase in MT number. We conclude that spatial or temporal regulation of MT dynamics during neuron polarization is not necessary to explain the accumulation of MTs in axons. Rather, the CLDM, which is the simplest possible model for MT DI, predicts a series of independent experiments by using a single consistent parameter set.

FRAP Experiments Confirm Complete MT Turnover in MPs and Axons

To directly test for the presence of stabilized or captured MTs, which are essential to the SSM but are not predicted to exist in the CLDM, we simulated FRAP experiments at the midpoint of MPs and at middle (AxMid) and distal (AxDist) locations in axons (Figures 4A and 4B; Movie S3). Using the parameter set obtained from the studies described above, the CLDM predicts faster recovery in the axon distal location than in the middle location and predicts that the MP and AxDist locations will have similar recovery halftimes, ~100 s (Figure 4D). In addition, the model predicts approximately 100% recovery at all locations (Figure 4E). The prediction of full recovery stands in marked contrast to the prediction of the SSM, which assumes that a subset of MTs is stably captured at their plus ends and therefore will not recover.

To test these model predictions, we performed FRAP experiments on EGFP-α-tubulin-expressing ECFNs. We found that α-tubulin turns over completely at all locations, before and after polarization, with half-times on the order of a few minutes (Figures 4C–4E). Axons had decreasing half-times of recovery and similar percent recoveries, from AxMid to AxDist, matching a priori simulation predictions (Figures 4D and 4E). Similarly, MPs had recovery half-times and percent recoveries that were not significantly different from those at the AxDist location, as predicted by the CLDM (p = 0.80; because of technical limitations, we were not able to measure FRAP recovery at a proximal axon location, data not shown). Complete turnover was observed experimentally at all three locations: 110% ± 18% in MPs, 102% ± 13% at AxMid, and 106% ± 9.6% at AxDist (mean ± 95% CI). The experimentally observed complete MT turnover at the AxMid and AxDist locations (Figure 4E), predicted by the CLDM, demonstrates that the SSM does not explain the ~3-fold increase in MTs in ECFN axons during polarization.

CLDM Predicts Experimentally Observed Age Distributions in MPs and Axons

Another test of the CLDM model is to predict the distribution of the average MT age along a neurite. Based on immunostaining

(J) Simulated EB1 distributions corresponding to all four examples of different V_D values shown in (F)–(I).

(K and L) Model distributions of growing MTs, with $V_D = -7.5$ nm/s, predict experimental EGFP-EB1 distributions in MPs (per 0.5 μm) (K) and axons (per 1.8 μm) (L) via the same MT DI parameters (growth and shortening rates, catastrophe and rescue frequencies) for both MPs and axons. Experimental data shown are mean ± 2 SEM (i.e., 95% confidence limits).

(M) The CLDM predicts a 3.5-fold increase in MT number via the same DI parameters for MPs and axons.

(N) The CLDM correctly predicts the percentage of retrogradely oriented EB1 comets in experimental MPs and axons. Simulation values in (M) and (N) are within 2 SEM of the experimental average value (i.e., within the 95% confidence limits), indicated by the shaded boxes. All of the experiments are consistent with a single set of DI parameters (see Table 1; $p > 0.05$).

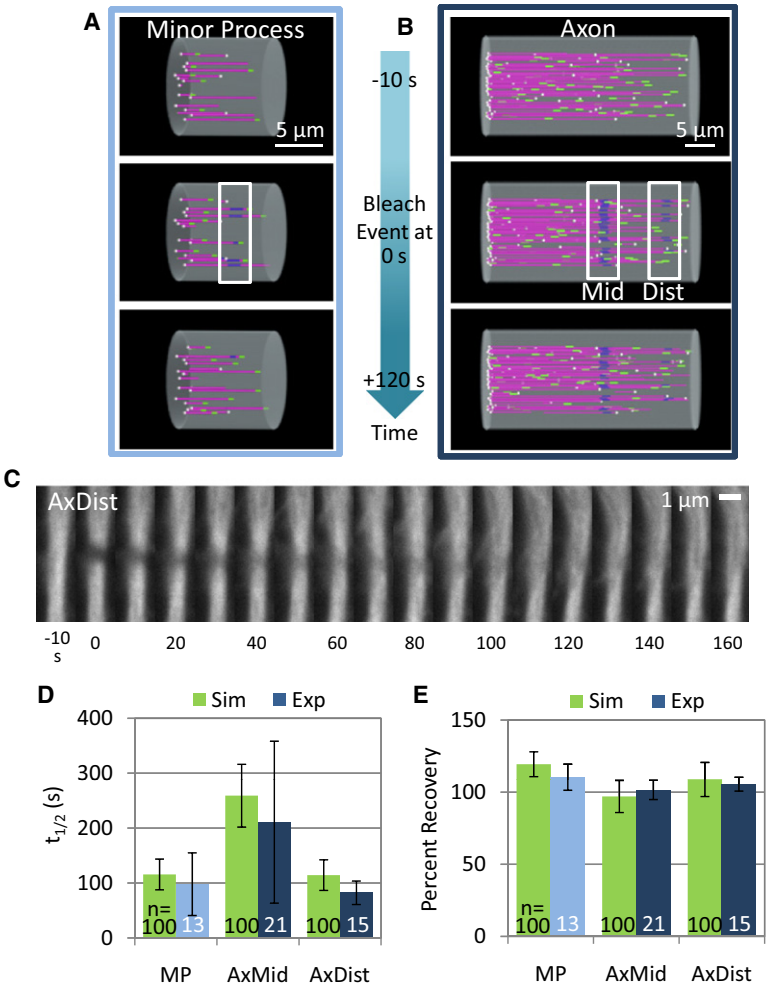

Figure 4. The Cell-Length-Dependent Model Predicts the Complete Turnover of MTs

(A and B) Animated depiction of simulated fluorescence recovery after photobleaching (FRAP) experiments in MPs (A) and axons (B). White boxes indicate photobleached regions. Photobleached MT regions are shown in dark purple, whereas unbleached MT regions are in magenta. Animation images from before, just after the bleach, and near full recovery are shown.

(C) Experimental montage of a FRAP experiment in the distal axon showing complete recovery near 160 s. The bleach event occurs at the zero time point.

(D and E) Model prediction and experimental results for half-time ($t_{1/2}$) of recovery (D) and percent recovery (E) of EGFP-α-tubulin during FRAP experiments. The cell-length-dependent model predicts similar half-times in the MPs and distally in the axon with a longer half-time predicted at the middle of the axon. Additionally, the model predicts complete recovery in MPs and in the distal axon and nearly complete recovery in the middle axon, all of which is observed experimentally. Number of simulations or FRAP experiments is shown in the bars in (D) and (E). Data shown are mean ± SEM.

for posttranslational tubulin modifications, tyrosination (newer MTs) and acetylation (older MTs), the SSM suggests that MTs are stabilized in axons because they are highly acetylated and because there is a higher ratio of acetylated to tyrosinated MTs as compared to MP MTs [4, 21, 22]. We found that the CLDM, again by using the same parameter set constrained by all of the above experiments, predicts a linearly decreasing distribution of mean MT age in MPs (Figure 5C). By contrast, the model predicts a small peak in MT age near the middle of the axon (Figure 5D). In addition, the simulation predicts that MTs will be older in axons as compared to MPs simply because of the increase in neurite length and the associated longer time required for the plus end to return to a given position along the MT (consistent with the tubulin FRAP half-time results in Figure 4D). The simulation also predicts abrupt changes in MT age along the length of an individual MT (Movie S4), which is consistent with previously observed abrupt transitions between tyrosinated and acetylated or detyrosinated immunostainings [23, 24]. Finally, the simulation demonstrates that the higher acetylation in axons (compared to MPs) does not necessarily imply a change in plus-end dynamics or imply that plus ends have been captured.

To determine whether the CLDM-predicted MT age distributions were present in the ECFNs, we examined the distribution of tyrosinated and acetylated MTs in immunostained neurons. Because both acetylated and tyrosinated MTs were found in both MPs and axons, we calculated the fluorescence intensity ratio of acetylated to tyrosinated (ace/tyr) MTs [4]. MPs stained brighter for newer MTs and had a decaying ace/tyr ratio (Figures 5A and 5C). In contrast, axons had an increased level of older MTs and had a small peak in the ace/tyr ratio near the middle of the axon, as predicted by the CLDM (Figures 5B and 5D) and consistent with previous experiments [25] and with the longer FRAP recovery at the AxMid location (Figure 4D). These experimental results quantitatively match the simulated predictions of MT age distributions in both MPs and axons. Based on the CLDM, we attribute the increased level of older MTs in the axon to the increased length of the axon.

We would like to note that the MP and axon exhibit different proportionalities of MT age relative to the ace/tyr age ratio, as observed in Figures 5C and 5D. For example, a 150 s mean MT age corresponds to an ace/tyr ratio of 1 in MPs and 2 in axons. An approximately 2-fold temporal increase in ace/tyr ratio was also previously observed in hippocampal neurons [4]. We attribute this difference in proportionality to time-dependent regulation of the acetylation cycle and detyrosination cycle kinetics. Equal half-times for MT turnover at the MP and AxDist locations measured via EGFP-α-tubulin FRAP, shown in Figure 4D, indicate similar MT dynamics at these two locations. However, the ace/tyr age ratio differs by a factor of 2 when the MP midpoint and AxDist locations are compared; see Figures 5C and 5D. The ace/tyr ratio does not appear to be a constant output of age over time, which reinforces the importance of measuring live MT dynamics. Even so, the axonal ace/tyr ratio is on average more than 2-fold higher than the MP ace/tyr ratio, again indicating increased age of axonal MTs relative to MP MTs.

The simulation age analysis demonstrates that MT plus ends can explore the axon for a longer amount of time simply because of the increased neurite length. This naturally generates MTs that are older and therefore have had time to accumulate the acetylation modification, which could lead to the generation of specialized MT tracks for cargo transport [26] during polarization.

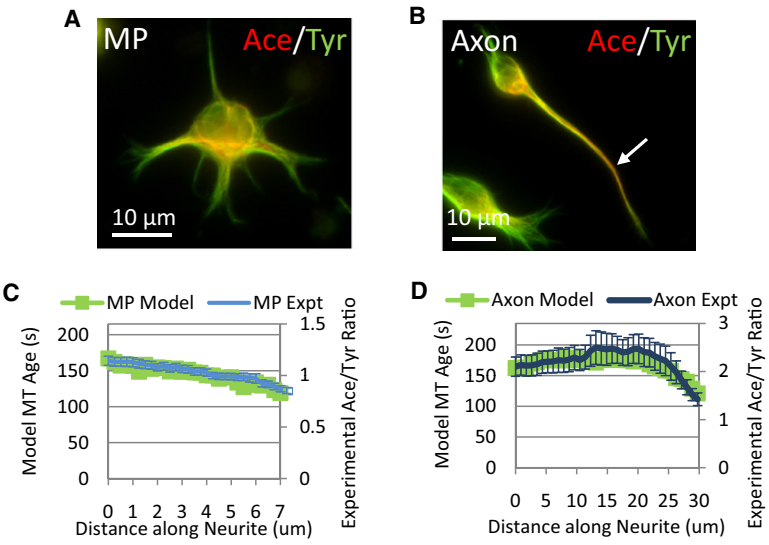

Figure 5. The Cell-Length-Dependent Model Predicts MT Age

(A and B) Example of dual immunostains for tyrosinated (newer, green) and acetylated (older, red) MTs in unpolarized MPs (A) and polarized axons (B). Tyrosinated MTs are abundant in GCs and at the distal ends of the neurites. Axons show greater acetylation staining near the middle of the axon, whereas MPs show little acetylated staining in general (n = 92 and n = 12 for MPs and axons, respectively).

(C and D) The cell-length-dependent model predicts MT age distributions in ECFNs (n = 100 simulations for MPs and axons), as assessed by the experimental distribution of acetylated/tyrosinated fluorescence intensity ratio in MPs (C) and axons (D). Data shown are mean ± SEM.

Discussion

We have identified a simple cell-length-dependent model to explain the observed MT accumulation during ECFN polarization. This model naturally explains how MTs can accumulate in one process as a function simply of the process length, which reinforces the importance of cell shape and size in controlling basic cellular processes [27–30]. The cell-length-dependent model does not necessarily exclude the possibility of selective stabilization, but it shows that selective stabilization is not required to achieve MT redistribution. In fact, the CLDM represents the base model upon which more sophisticated spatial and temporal regulation is potentially layered.

Modeling the MT dynamics in polarizing ECFNs led us to identify the MT arrival rate, $k_{arrival}$, as a key parameter. In particular, the steady-state number of MTs in a given process is determined solely by $k_{arrival}$ and the rate of MT plus-end departure (i.e., return to the cell body). Because the mean time spent by a plus end in a given process is approximately proportional to the process length, the steady-state number of MTs in the process will be proportional to both the arrival rate and the process length. We found that in the specific case of polarizing ECFNs, there was an overall 3.5-fold increase in MT number, even though the arrival rate increased only 1.7-fold. We then inferred an additional 2-fold increase that is accounted for quantitatively by the CLDM, with a slightly negative plus-end drift velocity ($V_D = -7.5$ nm/s for both MPs and axons). Thus, although increased arrival rate leads to an increase in ECFN axon MTs, it only partially accounts for the increase observed experimentally.

Taken together, our experimental results with ECFNs are consistent with the simple length-dependent model and demonstrate that alteration in net MT assembly is not necessary to promote axon specification in a particular MP. Instead, it appears that having more MTs to serve as tracks for motor-based delivery of signaling molecules (e.g., Par complex components [31]) is important in establishing and maintaining neuron polarity in a positive feedback loop with F-actin dynamics [32]. For example, in hippocampal neurons it has been shown that the GTPase HRas accumulates in the nascent axon via MT motor-dependent trafficking. HRas then participates in a positive feedback loop with PI3K to reinforce the nascent axon [33]. Similarly, it has been shown that accumulation of polarity-defining proteins like kinesin-1 [34] is dependent upon the length of the neurite. In Jacobson et al. [34], the minor process that underwent a growth spurt accumulated kinesin motors. This indicates that the longest neurite, which presumably had the most MTs, became the nascent axon.

Interestingly, it was also shown that accumulation of kinesin-1 [34] in a neurite does not immediately determine the nascent axon. Instead, transient accumulation of kinesin-1 in several different MPs was observed over time. This indicates that the feedback coupling between specifying the axis of polarity and the accumulation of polarity molecules must be relatively slow, otherwise the first MP to accumulate the polarity molecules or signal would immediately become the axon. This would cause neurons to polarize within tens of minutes rather than on the timescale of hours to days, which is observed experimentally. Therefore, it appears that the signaling mechanisms integrate over a period of hours to ultimately select the axon.

To determine what process lengths are relevant for the CLDM, we can use a dimensionless number known as the Péclet number (Pe), which parameterizes the relative importance of diffusion (D), drift (V_D), and system length scale (L) [35, 36]. For MTs in the CLDM, we define the Pe as $|V_D|L/D$, where the diffusion coefficient describes the underlying randomness of microtubule dynamics ($D = 2k_c k_r(V_g + V_s)^2/(k_c + k_r)^3 = 0.30\ \mu m^2/s$ [12]). If $Pe >> 1$, then drift is dominant and the MT plus ends will be exponentially clustered near $x = 0$ or $x = L$, depending on whether the drift is negative or positive, respectively. Conversely, if $Pe << 1$, then drift is negligible and the MT plus ends will be uniformly distributed along the x axis. For ECFN MTs, the Pe is 0.25 in MPs and 0.87 in axons, which means that drift is generally weak. However, if the axons were to continue to elongate with no change in MT dynamics, the Pe would exceed unity and drift would start to dominate. What is this length at which the Pe equals unity? From the definition of the Pe, we can define a decay length for the MT plus-end distribution via $Pe = L/L_{decay}$, where L is the cell length and $L_{decay} = D/V_D$ is the decay length. For both ECFN MPs and axons, we estimate the decay length $L_{decay} = 40\ \mu m$. For $V_D = -7.5$ nm/s, MTs in processes that are ~40 μm or less will exhibit the CLDM. However, should the axons continue to elongate to lengths $>> 40\ \mu m$ ($Pe >> 1$), there will be progressively less MT accumulation because centrosomally nucleated MT plus ends will fail to reach the growth cone and will thus lose their cell-length-dependent sensitivity. Therefore, for $V_D < 0$, Pe must be less than or close to 1 in order for the MTs to exhibit

the CLDM. Alternatively, if $V_D > 0$, then the CLDM will always apply regardless of the Pe because MTs will always reach the end of the process (although we note that the centrosome likely has a finite capacity to nucleate MTs, which will eventually limit MT accumulation). In general, the estimation of L_{decay} and Pe can be used in other cellular systems to determine a priori whether the CLDM would apply.

We also found that the CLDM is consistent with both early axotomy and neurite towing experiments. In axotomy experiments, transected axons whose relative length was >10 μm longer than the remaining processes remained the axon [37]. Conversely, if the transected axon was shorter than the remaining processes, the likelihood of remaining the axon was very low [37]. We simulated an axotomy experiment and found that the number of MTs decreased to MP levels over 20 min. In addition, we simulated neurite towing experiments [38], in which a second axon can be specified from a polarized neuron [39], and found that the number of MTs increased to axonal levels over 1.75 hr (Figure S8). These simulations demonstrate that the CLDM can explain axotomy and neurite towing results simply through cell-length-dependent changes in MT number.

Collectively, these results show that the cell-length-dependent model, absent of any spatial or temporal MT regulation, provides a straightforward mechanism to accumulate more MTs, and simultaneously generate older MTs, by increasing the length of the neurite, thus leading to cellular polarization. Although previous work in other cell types has shown that MTs are capable of exploring space until they reach a physical barrier [40], our work demonstrates that this exploration has consequences for the number of MTs oriented in a specific direction, especially during an important event such as cell polarization. Accumulation of MTs via neurite-length control may be a method by which neurons can accumulate polarity molecules faster in longer processes and can explain induced axon specification in neurite towing experiments [39]. We would like to note that these findings indicate that length-dependent MT accumulation is a default mechanism by which the cell increases MT numbers in response to cell shape changes. Any other method to accumulate MTs must therefore be superimposed on top of the default CLDM. We do not exclude the possibility for selective MT stabilization; however, it is not necessary for MT accumulation.

Our experimental results with ECFNs are consistent with the simple length-dependent model and demonstrate that alteration in net MT assembly is not necessary to promote axon specification in a particular MP. We posit that random F-actin protrusions in growth cones allow the MP or axon to detect the local concentration of adhesion molecules via a motor clutch mechanism [8, 20]. In this model, adhesive clutch bonds resist F-actin retrograde flow, thus allowing for preferential process extension in the direction of greatest adhesive resistance. This increased neurite length is then read out by the MT array via the CLDM, which can subsequently provide positive feedback to the F-actin cytoskeleton, for example via kinesin-based transport of the Ras and Par signaling components. Through this mechanism, the MTs, via spatially and temporally unbiased random searching, have a simple way to read out changes in cell length and thereby mediate cell polarization.

Experimental Procedures

Simulation of MT Dynamics in a Neurite

MT DI was simulated as described in Sprague et al. [41]. Briefly, with 200 ms time steps (Δt) and 12 nm spatial steps (i.e., pixels), MTs are allowed to grow at a rate V_g and shorten at a rate V_s. The following equation was used to determine the probability of a catastrophe or rescue: P(switch event) = $1 - \exp(-k \times \Delta t)$, where k is the frequency of either catastrophe (k_c) or rescue (k_r), depending on the growth state of the MT.

If the length added or lost during one time step was not exactly divisible by the pixel size, resulting in a decimal value, then we implemented a stochastic approach to determining how much length should be added or lost. The nearest whole lengths above and below the decimal value were used, and appropriate probabilities were assigned to each such that, on average, the length added or lost is close to the actual decimal value. At each time step, a random number was generated and one of the two nearest integer values was chosen. Implementing this stochastic determination of lengths added or lost allowed us to avoid large rounding errors in the simulation and keep our pixel size constant.

To simulate MT dynamics in a neurite, we allowed MTs to grow to the growth cone edge, which was length $L_{neurite}$ away from the cell body. MTs that grew to the growth cone edge immediately underwent catastrophe. Anterogradely oriented MTs arrived from the cell body at rate $k_{arrival}$. MTs were also nucleated at the rate k_{nuc} uniformly along the length of the neurite, with an equal probability of being oriented either anterogradely or retrogradely. Retrogradely oriented MTs were allowed to grow into a 10 μm diameter cell body. MTs that grew the entire diameter of the cell body immediately underwent catastrophe.

The value of $k_{arrival}$ used in the simulation was constrained so that the chosen value was within ±2 times the SEM of the mean value (i.e., $p > 0.05$). Similarly, the simulation prediction of the percentage of retrogradely oriented EB1 comets and the number of MTs at the proximal neurite base (at x = 0) had to be within 2 SEM of the experimentally observed mean value.

To analyze the simulated MT dynamics, we used data only from the neurite shaft, not the growth cone, for comparison to experimental results. Based on experimental measurements, growth cones were on average 3 or 5 μm long for minor processes and axons, respectively.

MT distributions from the simulations were calculated by summing the number of MTs, including nucleated MTs, along the neurite and constructing a histogram. EB1 or growing MT distributions were calculated in a similar manner.

Simulated MT age was analyzed by dividing the neurite into evenly spaced bins. For each bin and simulation, the average time for a single MT to grow into a bin and then shorten out of that same bin was calculated to obtain the MT age distribution along the neurite.

Animations were generated by using a custom code in OpenDX (http://opendx.org/).

Transfection, Cell Culture, and Constructs

On embryonic day 5 or 6, chick embryos were transfected via in ovo electroporation as previously described [20]. At E7 or E8, electroporated embryos were dissected according to published procedure [38]. Briefly, the electroporated forebrain hemisphere was dissected, trypsinized, and dissociated via trituration. Cells were resuspended in F12 media with fetal bovine serum, plated onto prepared PEI-coated glass bottom dishes (Mattek; [38]), and incubated in a 37°C air incubator.

The following constructs were used: pEGFP-EB1 and pEGFP-γ-tubulin (gifts from L. Cassimeris; [42]), pEGFP-α-tubulin (Clontech), pEGFP-β-actin (a gift from P.C. Letourneau), and pmCherry-β-actin and pmCherry (gifts from R.Y. Tsien; [43]).

Immunocytochemistry

For endogenous EB1 immunostaining, cultured untransfected ECFNs were fixed with −20°C methanol for 5 min. Rabbit anti-EB1 monoclonal antibody (1:10,000; Sigma, E3406) was used, followed by the Alexa 488 goat anti-rabbit secondary antibody (1:10,000; Invitrogen, A11070).

For β-tubulin, acetylated and tyrosinated MT immunostaining cells underwent simultaneous fixation and extraction, to remove free tubulin dimers, in PHEM buffer (60 mM Pipes, 25 mM HEPES, 5 mM EGTA, and 1 mM MgCl) containing 0.25% glutaraldehyde, 3.7% paraformaldehyde, 3.7% sucrose, and 0.1% Triton X-100 [4]. The following primary antibodies were used: anti-β-tubulin (mouse clone TUB 2.1, 1:1000; Sigma-Aldrich), anti-acetylated tubulin (clone 6-11B-1, 1:4000; Sigma-Aldrich), and anti-tyrosinated tubulin YL1/2 (1:640; Abcam). Labeled samples were imaged with a Nikon TE200, CoolSnap HQ2 cooled charge-coupled device camera (Photometrics), and MetaMorph software v.7.02 (Molecular Devices). Additional details can be found in the Supplemental Experimental Procedures.

Microscopy and Image Processing

Live fluorescence time-lapse images were acquired 4–40 hr after plating, as previously described [20]. Briefly, a 1.49NA 60× Plan Apo TIRF objective and a 2.5× projection lens were used, giving a final pixel size of 42 nm. Single and dual channel imaging was acquired at 1 and 2 s intervals, respectively. Images were acquired with a CoolSnap HQ2 camera. EGFP (49002) and dual EGFP/TRITC (52004v2) or EGFP/mCherry (59222) filter sets from Chroma were used. Image acquisition was controlled by MetaMorph v.7.02. Additional details can be found in the Supplemental Experimental Procedures.

FRAP Experiments

FRAP experiments were performed on EGFP-α-tubulin-expressing ECFNs. Neurites were imaged at 10 s intervals for 10 frames and then bleached for 5 ms with a 25 mW Argon-ion laser beam focused to ~1 um in width (Spectraphysics). The recovery was captured for another 10 min at 10 s intervals. Imaging and bleaching were controlled via a custom journal in MetaMorph. Additional details can be found in the Supplemental Experimental Procedures.

Calculation of EB1 Comet Velocities and Lifetimes

EB1 comets in fluorescence time-lapse movies were tracked manually by clicking on the brightest part of the comet. The ImageJ v1.37 (http://rsbweb.nih.gov/ij/) manual tracking plugin was used to record the coordinates of each click and the number of MTs tracked. Using the manual tracking data, we calculated frame-to-frame instantaneous velocities and comet lifetimes via a custom MATLAB code. Comet lifetime is defined as the amount of time a comet was tracked before it disappeared. The sign of an instantaneous velocity measurement was determined by comparing the distance traveled, relative to a reference point, of the current time point to the previous time point.

To determine the error associated with manually clicking on the brightest point of the comet, we constructed a simulated comet moving at a constant velocity of 150 nm/s, comparable to experimentally observed rates, in MATLAB. An exponential decay was used to model the comet fluorescence intensity decay. The simulated comet was model convolved [41, 44, 45], and noise was added to each image to simulate experimental images of EB1 comets. The clicking error was measured to be 40 nm, which is equivalent to the camera pixel size of 42 nm.

Measurement of Microtubule and EB1 Distributions

MT distributions were measured with extracted β-tubulin immunostained ECFNs to remove most of the tubulin monomer. EB1 distributions were estimated with dual transfected EGFP-EB1 and mCherry ECFNs. mCherry was used as a volume marker, as described in Bulinski et al. [46], to subtract the free EGFP-EB1 signal from the bound signal, resulting in an image of only comets. This technique was attempted with EGFP-α-tubulin ECFNs, but MTs were too dense to find a cellular location devoid of MTs. The distribution of MTs and EB1 comets was measured by using the Linescan function in MetaMorph, starting at the proximal end of the neurite where the neurite began to have a uniform caliber. The end of the neurite was defined to be the distal end of the growth cone where the bulk of the peripheral domain ended, not including any protruding filopodia.

Statistical Analysis

An F test was used to determine whether the various comet velocity and lifetime groups were different from each other (Figures 3D and 3E). Rejection of the null hypothesis, in the case of comparison between comet velocities, was followed by multiple comparison testing with the Tukey-Kramer test for unequal observations to determine which groups were different from each other. An alpha of 0.01 was used for multiple comparison testing. Comparisons between the means of two groups were made via Student's t test. The statistical toolbox in MATLAB R2006a was used to perform all statistical tests.

For practical reasons, only significance found between the same cellular compartment during polarization (i.e., stage 2 CB and stage 3 CB, or MP and Ax) or within the same polarization state (i.e., stage 2 CB, MPs and MPGCs) was considered important. Significance between dissimilar cellular compartments in different polarization states (i.e., stage 2 CB and Ax) was disregarded because it lacked any apparent practical meaning.

Supplemental Information

Supplemental Information includes Supplemental Experimental Procedures, eight figures, and four movies and can be found with this article online at doi:10.1016/j.cub.2010.04.040.

Acknowledgments

Thanks to M.G. Blackmore, J.L. Harder, and N. Koyano for assistance with in ovo electroporation and M.K. Gardner and C.E. Chan for assistance with MATLAB. Thanks to L. Cassimeris, P.C. Letourneau, and R.Y. Tsien for the plasmid gifts. We also thank P.C. Letourneau, B. Marsick, and D. Bray for helpful discussions. Supported by National Science Foundation grant MCB-0615568.

Received: November 6, 2009
Revised: April 19, 2010
Accepted: April 21, 2010
Published online: May 20, 2010

References

1. Li, R., and Gundersen, G.G. (2008). Beyond polymer polarity: How the cytoskeleton builds a polarized cell. Nat. Rev. Mol. Cell Biol. *9*, 860–873.
2. Mitchison, T., and Kirschner, M. (1984). Dynamic instability of microtubule growth. Nature *312*, 237–242.
3. Gundersen, G.G., and Bulinski, J.C. (1988). Selective stabilization of microtubules oriented toward the direction of cell migration. Proc. Natl. Acad. Sci. USA *85*, 5946–5950.
4. Witte, H., Neukirchen, D., and Bradke, F. (2008). Microtubule stabilization specifies initial neuronal polarization. J. Cell Biol. *180*, 619–632.
5. Kirschner, M., and Mitchison, T. (1986). Beyond self-assembly: From microtubules to morphogenesis. Cell *45*, 329–342.
6. Palazzo, A.F., Cook, T.A., Alberts, A.S., and Gundersen, G.G. (2001). mDia mediates Rho-regulated formation and orientation of stable microtubules. Nat. Cell Biol. *3*, 723–729.
7. Niethammer, P., Bastiaens, P., and Karsenti, E. (2004). Stathmin-tubulin interaction gradients in motile and mitotic cells. Science *303*, 1862–1866.
8. Mitchison, T., and Kirschner, M. (1988). Cytoskeletal dynamics and nerve growth. Neuron *1*, 761–772.
9. Hill, T.L. (1981). Microfilament or microtubule assembly or disassembly against a force. Proc. Natl. Acad. Sci. USA *78*, 5613–5617.
10. Vorobjev, I.A., Rodionov, V.I., Maly, I.V., and Borisy, G.G. (1999). Contribution of plus and minus end pathways to microtubule turnover. J. Cell Sci. *112*, 2277–2289.
11. Gardner, M.K., Bouck, D.C., Paliulis, L.V., Meehl, J.B., O'Toole, E.T., Haase, J., Soubry, A., Joglekar, A.P., Winey, M., Salmon, E.D., et al. (2008). Chromosome congression by Kinesin-5 motor-mediated disassembly of longer kinetochore microtubules. Cell *135*, 894–906.
12. Verde, F., Dogterom, M., Stelzer, E., Karsenti, E., and Leibler, S. (1992). Control of microtubule dynamics and length by cyclin A- and cyclin B-dependent kinases in Xenopus egg extracts. J. Cell Biol. *118*, 1097–1108.
13. v Kampen, N.G. (1981). Stochastic Processes in Physics and Chemistry (Amsterdam: Elsevier).
14. Heidemann, S.R., Reynolds, M., Ngo, K., and Lamoureux, P. (2003). The culture of chick forebrain neurons. Methods Cell Biol. *71*, 51–65.
15. Yu, W., and Baas, P.W. (1994). Changes in microtubule number and length during axon differentiation. J. Neurosci. *14*, 2818–2829.
16. Tirnauer, J.S., and Bierer, B.E. (2000). EB1 proteins regulate microtubule dynamics, cell polarity, and chromosome stability. J. Cell Biol. *149*, 761–766.
17. Ligon, L.A., Shelly, S.S., Tokito, M., and Holzbaur, E.L. (2003). The microtubule plus-end proteins EB1 and dynactin have differential effects on microtubule polymerization. Mol. Biol. Cell *14*, 1405–1417.
18. Dotti, C.G., Sullivan, C.A., and Banker, G.A. (1988). The establishment of polarity by hippocampal neurons in culture. J. Neurosci. *8*, 1454–1468.
19. Stepanova, T., Slemmer, J., Hoogenraad, C.C., Lansbergen, G., Dortland, B., De Zeeuw, C.I., Grosveld, F., van Cappellen, G., Akhmanova, A., and Galjart, N. (2003). Visualization of microtubule growth in cultured neurons via the use of EB3-GFP (end-binding protein 3-green fluorescent protein). J. Neurosci. *23*, 2655–2664.
20. Chan, C.E., and Odde, D.J. (2008). Traction dynamics of filopodia on compliant substrates. Science *322*, 1687–1691.
21. Gomis-Rüth, S., Wierenga, C.J., and Bradke, F. (2008). Plasticity of polarization: Changing dendrites into axons in neurons integrated in neuronal circuits. Curr. Biol. *18*, 992–1000.
22. Ferreira, A., Busciglio, J., and Cáceres, A. (1989). Microtubule formation and neurite growth in cerebellar macroneurons which develop

in vitro: Evidence for the involvement of the microtubule-associated proteins, MAP-1a, HMW-MAP2 and Tau. Brain Res. Dev. Brain Res. *49*, 215–228.

23. Baas, P.W., and Black, M.M. (1990). Individual microtubules in the axon consist of domains that differ in both composition and stability. J. Cell Biol. *111*, 495–509.
24. Brown, A., Li, Y., Slaughter, T., and Black, M.M. (1993). Composite microtubules of the axon: Quantitative analysis of tyrosinated and acetylated tubulin along individual axonal microtubules. J. Cell Sci. *104*, 339–352.
25. Baas, P.W., Ahmad, F.J., Pienkowski, T.P., Brown, A., and Black, M.M. (1993). Sites of microtubule stabilization for the axon. J. Neurosci. *13*, 2177–2185.
26. Cai, D., McEwen, D.P., Martens, J.R., Meyhofer, E., and Verhey, K.J. (2009). Single molecule imaging reveals differences in microtubule track selection between Kinesin motors. PLoS Biol. *7*, e1000216.
27. Meyers, J., Craig, J., and Odde, D.J. (2006). Potential for control of signaling pathways via cell size and shape. Curr. Biol. *16*, 1685–1693.
28. Moseley, J.B., Mayeux, A., Paoletti, A., and Nurse, P. (2009). A spatial gradient coordinates cell size and mitotic entry in fission yeast. Nature *459*, 857–860.
29. Terenna, C.R., Makushok, T., Velve-Casquillas, G., Baigl, D., Chen, Y., Bornens, M., Paoletti, A., Piel, M., and Tran, P.T. (2008). Physical mechanisms redirecting cell polarity and cell shape in fission yeast. Curr. Biol. *18*, 1748–1753.
30. Guilak, F., Cohen, D.M., Estes, B.T., Gimble, J.M., Liedtke, W., and Chen, C.S. (2009). Control of stem cell fate by physical interactions with the extracellular matrix. Cell Stem Cell *5*, 17–26.
31. Nishimura, T., Kato, K., Yamaguchi, T., Fukata, Y., Ohno, S., and Kaibuchi, K. (2004). Role of the PAR-3-KIF3 complex in the establishment of neuronal polarity. Nat. Cell Biol. *6*, 328–334.
32. Shi, S.H., Jan, L.Y., and Jan, Y.N. (2003). Hippocampal neuronal polarity specified by spatially localized mPar3/mPar6 and PI 3-kinase activity. Cell *112*, 63–75.
33. Fivaz, M., Bandara, S., Inoue, T., and Meyer, T. (2008). Robust neuronal symmetry breaking by Ras-triggered local positive feedback. Curr. Biol. *18*, 44–50.
34. Jacobson, C., Schnapp, B., and Banker, G.A. (2006). A change in the selective translocation of the Kinesin-1 motor domain marks the initial specification of the axon. Neuron *49*, 797–804.
35. Crank, J. (1979). The Mathematics of Diffusion, Second Edition (Oxford: Clarendon Press).
36. Bird, R.B., Stewart, W.E., and Lightfoot, E.N. (2007). Transport Phenomena, Revised Second Edition (New York: J. Wiley).
37. Goslin, K., and Banker, G. (1989). Experimental observations on the development of polarity by hippocampal neurons in culture. J. Cell Biol. *108*, 1507–1516.
38. Fass, J.N., and Odde, D.J. (2003). Tensile force-dependent neurite elicitation via anti-beta1 integrin antibody-coated magnetic beads. Biophys. J. *85*, 623–636.
39. Lamoureux, P., Ruthel, G., Buxbaum, R.E., and Heidemann, S.R. (2002). Mechanical tension can specify axonal fate in hippocampal neurons. J. Cell Biol. *159*, 499–508.
40. Komarova, Y.A., Vorobjev, I.A., and Borisy, G.G. (2002). Life cycle of MTs: Persistent growth in the cell interior, asymmetric transition frequencies and effects of the cell boundary. J. Cell Sci. *115*, 3527–3539.
41. Sprague, B.L., Pearson, C.G., Maddox, P.S., Bloom, K.S., Salmon, E.D., and Odde, D.J. (2003). Mechanisms of microtubule-based kinetochore positioning in the yeast metaphase spindle. Biophys. J. *84*, 3529–3546.
42. Piehl, M., and Cassimeris, L. (2003). Organization and dynamics of growing microtubule plus ends during early mitosis. Mol. Biol. Cell *14*, 916–925.
43. Shaner, N.C., Campbell, R.E., Steinbach, P.A., Giepmans, B.N., Palmer, A.E., and Tsien, R.Y. (2004). Improved monomeric red, orange and yellow fluorescent proteins derived from Discosoma sp. red fluorescent protein. Nat. Biotechnol. *22*, 1567–1572.
44. Sprague, B.L., Gardner, M.K., Pearson, C.G., Maddox, P.S., Bloom, K., Salmon, E.D., and Odde, D.J. (2004). Model-convolution approach to modeling fluorescent protein dynamics. Signals, Systems and Computers. Conference Record of the Thirty-Eighth Asilomar Conference, *2*, 1821–1825.
45. Gardner, M.K., Odde, D.J., and Bloom, K. (2007). Hypothesis testing via integrated computer modeling and digital fluorescence microscopy. Methods *41*, 232–237.
46. Bulinski, J.C., Odde, D.J., Howell, B.J., Salmon, T.D., and Waterman-Storer, C.M. (2001). Rapid dynamics of the microtubule binding of ensconsin in vivo. J. Cell Sci. *114*, 3885–3897.